The Effect of the Acceleration Voltage on the Quality of Structure Determination by 3D-Electron Diffraction

Saleh Gholam[a], Joke Hadermann[a]*

[a] EMAT, University of Antwerp, Groenenborgerlaan 171, Antwerp 2020, Belgium

*Corresponding author

Abstract

Nowadays, 3D Electron Diffraction (3DED) is widely used for the structure determination of sub-micron-sized particles. In this work, we investigate the influence of the acceleration voltage on the quality of 3DED datasets acquired on $BaTiO_3$ nanoparticles. Datasets were acquired using a wide range of beam energies, from common, high acceleration voltages (300 kV and 200 kV) to medium (120 kV and 80 kV) and low acceleration voltages (60 kV and 30 kV). In the integration process, R_{int} increases as the beam energy reduces, which is mainly due to the increased dynamical scattering. Nevertheless, the structure was solved successfully in all cases. The structure refinement was comparable for all beam energies with small deficiencies such as negative atomic displacements for the heaviest atom in the structure, barium. Including extinction correction in the refinement noticeably improved the model for low acceleration voltages, probably due to higher beam absorption in these cases. Dynamical refinement, however, shows superior results for higher acceleration voltages, since the dynamical refinement calculations currently discard inelastic scattering effects.

Keywords

3D electron diffraction (3DED); structure solution; structure refinement; transmission electron microscope (TEM)

1 Introduction

During the last decade, 3D Electron Diffraction (3DED) has demonstrated promising results for studying the atomic structure of nanomaterials using transmission electron microscopes (TEMs). It has been applied to various classes of materials, ranging from materials sciences to life sciences [1, 2]. Even though there is extensive literature on the different 3DED methods and the involved parameters [3, 4], the beam energy is often overlooked as a tunable parameter. This might be because most TEM labs usually operate at a fixed, high acceleration voltage, such as 200 kV or 300 kV. These high beam energies provide some advantages for imaging techniques such as less distortion of the lenses and higher penetration depth as well as less beam broadening and higher spatial resolution in the scanning techniques [4, 5]. Consequently, a substantial majority of the 3DED studies have also used these conventional energies for structure determination. Higher energies than 300 kV are not conventional on modern TEMs mainly due to the high instrumental and operational costs, low high-voltage stability, parasitic aberrations and high probability of radiation damage [5]; nevertheless, there are no technical issues for operating TEMs at energies lower than 200 kV. By lowering the beam energy, the interaction of the electrons with the matter intensifies, as both elastic and inelastic cross-sections increase [6]. This increased cross-section can be helpful for analyzing small nanoparticles, as the scattering signal intensifies at lower energies. Although using lower energies is rare in 3DED studies, there are several studies showing excellent structure determination for minerals [7-9] and even organic compounds [10, 11] at 120 kV. It is worth noting that the very initial attempts for solving structures by electron diffraction were performed using diffractometers operating at 50 kV and TEMs at 80 kV [12, 13]. These studies used in-zone diffraction patterns which possess high dynamical scattering, yet showed decent accuracy.

Nonetheless, lowering the beam energy will have consequences on the 3DED experiments which should be taken into account. Firstly, the distortions of the lenses worsen as the beam energy decreases in a TEM [14]. Theoretically, when an electron beam propagates through lenses, it suffers a phase shift $\chi(u)$, defined as:

$$\chi(u) = \pi \Delta f \lambda u^2 + \frac{1}{2}\pi C_s \lambda^3 u^4 \qquad \text{(eq. 1-1)}$$

In this equation, u, $\Delta f, C_s$ and λ are the reciprocal-lattice vector, defocus, spherical aberration and wavelength, respectively. Based on this, at zero defocus, the lens distortions are proportional to the wavelength to the power of 3. Thus, for instance, the distortions are expected to be more than 15 times higher at 60 kV compared to 300 kV for the same microscope. Although the distortions can deteriorate the resolution in conventional imaging techniques, they merely affect the position of the Bragg reflections in diffraction, and it is possible to calculate and take these distortions into account during 3DED data treatment [15-18].

Secondly, the mechanisms of beam damage alter depending on the beam energy. At higher energies, elastic interactions can occasionally induce knock-on damage in metals, semiconductors and insulators [5], whereas, at lower energies, higher inelastic scattering can result in radiolytic processes, electrostatic charging or heating effects, raising concerns for mainly biological and organic samples [19]. For inorganic compounds, the concerns can be somewhat relaxed in 3DED studies since diffraction studies require much lower doses compared to conventional imaging techniques [20].

Thirdly, a higher elastic scattering cross-section can lead to higher dynamical/multiple scattering at lower beam energies. This can be also observed in the extinction distance parameter:

$$\xi_u = \frac{\pi \Omega cos\theta_B}{\lambda F_u} \quad \text{(eq. 1-2)}$$

where u is the diffraction vector, Ω is the volume of the unit cell, θ_B is the Bragg angle, λ is the wavelength of the electron beam and F_u is the structure factor for reflection u. At lower beam energies, the extinction distance decreases due to the increase in the wavelength and the Bragg angle. Thus, the multiple scattering at a certain thickness and orientation of the sample should be different for different beam energies. This can challenge the structure solution algorithms. In this context, inelastic scattering can play a beneficial role. Based on theoretical studies, a large portion of the inelastically scattered electrons still travel in the direction of Bragg reflections and are mainly kinematic. Thus, inelastic scattering can benefit the structure solution in these cases [20]. Nevertheless, 3DED studies utilizing energy filtration have shown better results compared to non-filtered data [21, 22]. These results might seem contradictory, but the thickness of the sample plays an important role in the cumulative portions of kinematically to dynamically scattered electrons according to the theoretical calculations. Thicker samples also increase the portion of inelastically scattered electrons which do not end up in Bragg spots. These can fade weak reflections at higher resolutions. An energy filter resolves these weak reflections. It should be also noted that using an energy filter does not remove all inelastic effects, since energy losses by phonons can be lower than 1 eV. Thus, the experimental and theoretical results are not necessarily contradictory.

Lastly, as mentioned earlier, the increased inelastic scattering can dissipate the signal of the Bragg reflections. It was observed that a good signal is acquired from a protein sample having twice the thickness of its inelastic mean free path (2×In-MFP) at 120 kV, 200 kV and 300 kV. Increasing the thickness to 3×In-MFP reduced the resolution in all mentioned energies, making the data treatment problematic, and thicker specimens did not show any useful signal [11]. In the case of inorganic samples, these thresholds increase, since these compounds have higher effective atomic numbers than proteins. This reduces the ratio of the inelastic to elastic scattering in inorganics.

In this study, we investigate the influence of the acceleration voltage of the TEM on the structure determination using the 3DED method. We explore the use of beam energies ranging from 30 kV to 300 kV, on commercial $BaTiO_3$ nanoparticles. The structure could be solved for all beam energies. This result demonstrates the potential of the 3DED method to be used in a wide range of beam energies, down to those used by conventional scanning electron microscopes (SEMs). The quality of the data was compared in detail during data reduction or integration, kinematical refinement and dynamical refinement. Inelastic scattering and dynamical scattering appear to play the main roles in altering the quality of the data.

2 Experimental

2.1 Microscopes

3DED experiments were performed on an FEI Tecnai Osiris transmission electron microscope at 30 and 200 kV and an FEI Titan TEM at 60, 120, and 300 kV (referred to respectively as TEM 1 and TEM 2 in this paper), using a Fischione tomography holder. To

perform experiments at 30 kV, a full gun and column alignment was performed on TEM 1. The alignment was followed according to the default steps and manual provided in FEI user interface. To improve the alignment, the steps were repeated 3 times. The rest of the experiments were performed using factory-made alignment files.

TEM 2 is equipped with a probe corrector and 3 condenser lenses, versus 2 lenses for TEM 1. This provides a parallel beam in a larger illumination range in the TEM mode. Both microscopes are equipped with a US1000 XP CCD camera (Gatan). Diffraction patterns were acquired by using a 20-µm C2 aperture in TEM mode using microprobe mode. The tomography experiments were performed by tilting the stage continuously at 0.437 deg/s, using an in-house written Python script. No particle tracking was used for the data acquisition, thus the beam was spread as much as possible to keep the particle under illumination during the tomography series. The diffraction patterns were recorded by the CCD in the continuous mode. Consequently, 10 % of the data was lost due to the read-out time of the detector at the end of each frame. This was taken into account for the data treatment.

2.2 Materials

3DED datasets were collected from $BaTiO_3$ nanoparticles (Batch No. MKCJ6201 Sigma-Aldrich). The nanoparticles were cubes with 40 – 50 nm size. They were dispersed in ethanol (Sigma-Aldrich) using an ultrasonic bath for 15 mins. 3 droplets of this solution were deposited on carbon support grids. To reduce the diffuse scattering in the background, the datasets were acquired using copper grids with a lacey carbon support (Electron Microscopy Sciences) at TEM 1 and an ultra-thin, continuous carbon support (Electron Microscopy Sciences) at TEM 2. 2 particles were analyzed at each microscope at the mentioned acceleration voltages.

2.3 Data Analysis

For the data analysis, images with TIF format were created from sets of EMI and SER files using Hyperspy [23]. The 3DED datasets were treated using PETS2 software for the integration of the intensities [24], which includes peak finding, unit cell determination, distortion refinement, indexation, frame geometry optimization and the integration of the intensity profile. The final integration was performed via the fit profile feature in PETS2 in combination with scaling the frames. The structure solution was performed using charge flipping through Superflip [25] incorporated in Jana2020 [26]. The kinematical and dynamical structure refinements were also performed using Jana2020.

3 Results and Discussion

3.1 Data Reduction

3DED datasets were acquired at the maximum possible ranges, which depended on practical factors such as the location of the particle on the grid and the surrounding particles. To have a valid comparison between the datasets of each particle, the analyses were limited to the smallest angular range and resolution among the different datasets, as listed in Table 1.

Table 1. The ranges of the datasets for each particle.

Particle	Acceleration Voltages (kV)	Range (deg)
P1	30, 200	-30 to 50
P2	30, 200	-30 to 50
P3	60, 120, 300	-60 to 45
P4	60, 120, 300	-60 to 50

After the peak search, a cubic unit cell was found in all datasets with some deviations which can be due to the distortions on the data. Nevertheless, it is known that $BaTiO_3$ nanoparticles demonstrate slight, local tetragonality [27]. This tetragonality is due to the dislocation of the titanium atom from the center of the unit cell (Figure 1). Consequently, there is a slight shift in the position of one oxygen atom and a slight change in the length of the unit cell. However, this titanium delocalization is not homogenous over the whole nanoparticle [28]. Therefore, this minor difference might not be pronounced in the 3DED signal as it represents the whole particle on average. In the supplementary data, we demonstrate that our data do not show any strong evidence that the unit cell is tetragonal and has to be solved and refined in the $P4mm$ space group instead of the cubic space group $Pm\bar{3}m$. Therefore, in this paper, the unit cell is considered to be cubic.

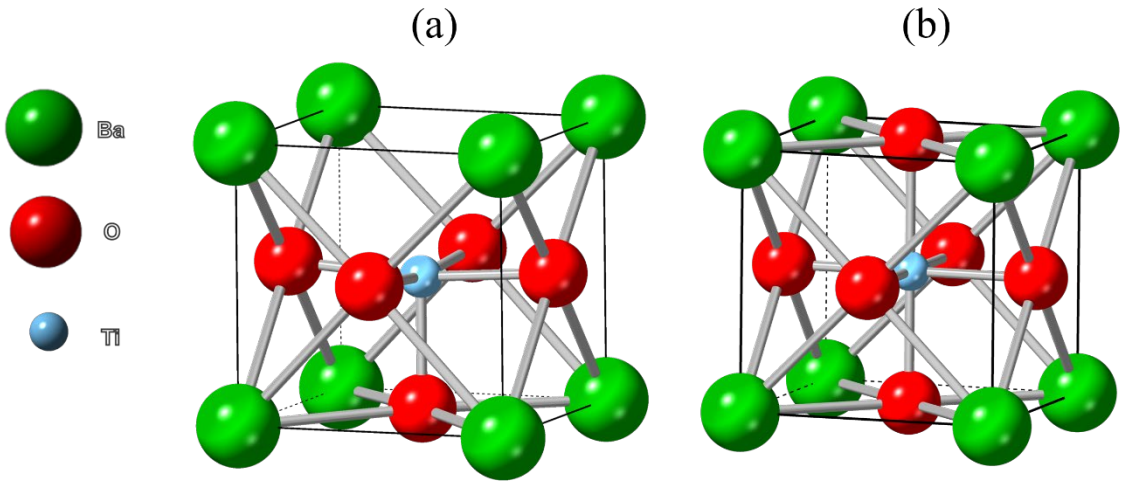

Figure 1. $BaTiO_3$ unit cell in (a) tetragonal and (b) cubic system.

The distortion refinement was performed on all datasets using cubic symmetry constraints. To overcome the difficulties in the integration process for datasets with higher distortions, the refinement of the general distortions of the data and the frame geometry optimization was repeated a few times. The process was evaluated by the noisiness of the average camel plot and the dispersion of the clusters of reflections in the cylindrical projection (Figure 2). In the end, the unit cell lengths of the datasets were 4.03 ± 0.01 Å. The absolute values for each type of distortion are plotted for each dataset in Figure 3. As expected, there is a general ascending trend in each type of distortion for each microscope by decreasing the acceleration voltage. The elliptical distortions of TEM 1 do not follow this trend. This can be due to the dependence of elliptical distortions on the alignments of the diffraction astigmatism by the user.

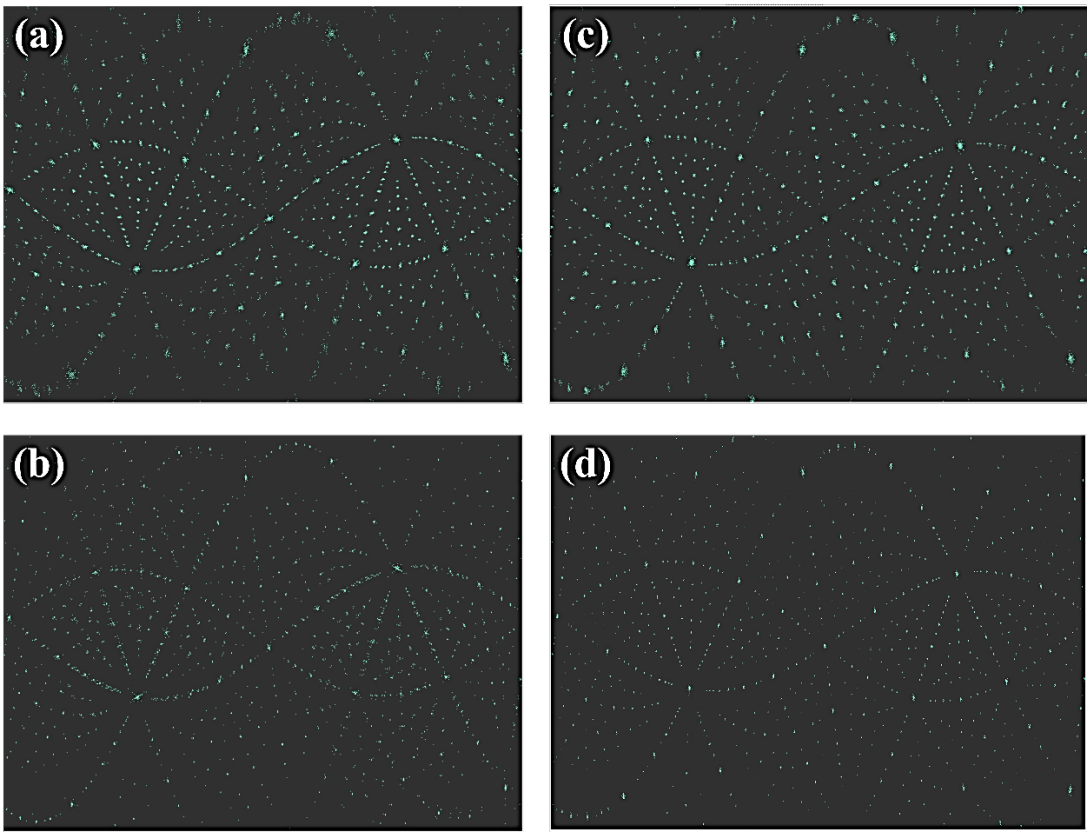

Figure 2. Cylindrical projection of the reflections for P1 at 200 kV (a and b) and 30 kV (c and d). The top row is before and the bottom row is after the optimization of frame geometry and distortion refinement.

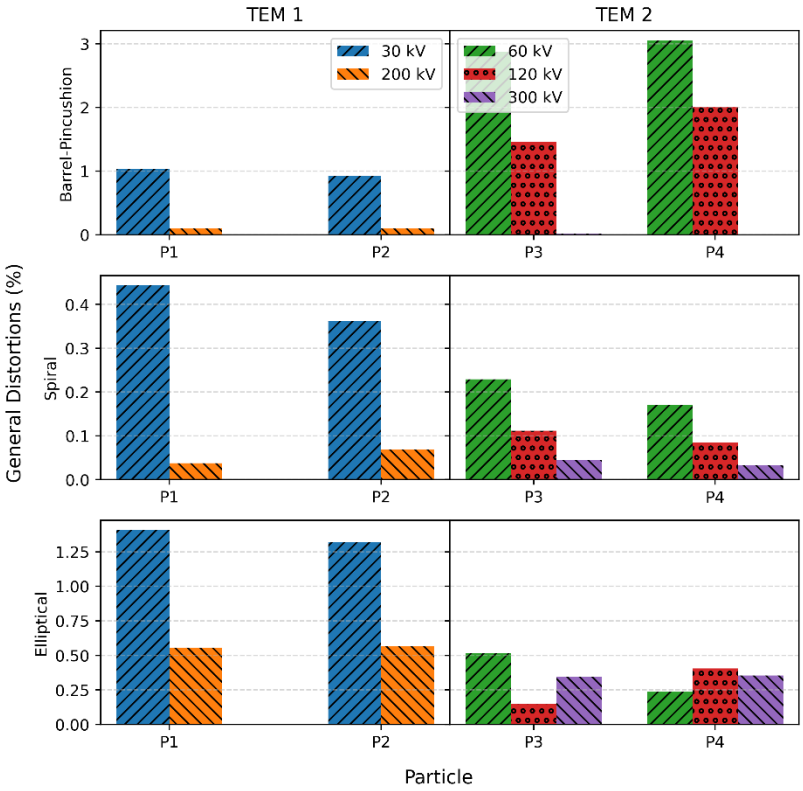

Figure 3. General distortion values after refinement for TEM 1 (left) and TEM 2 (right).

As a measure of the overall quality of the integration process, we compare the reliability factor for the symmetrically equivalent reflections (R_{int}) in these datasets. As observed in Figure 4, there is an ascending trend in R_{int} as the acceleration voltage decreases. This could originate from intrinsic or extrinsic differences in these experiments. Extrinsic differences do not originate from the nature of the beam energy, but due to some experimental differences which cause errors in the comparison between datasets. For instance, a different electron dose (i.e. signal-to-noise ratio), coverage of some reflections by the beam-stop, or the intense background signal at lower voltages can induce some differences from one experiment to the other. The latter is particularly significant in the case of TEM 2 data because of using continuous grids (P3 on Figure 5). Moreover, the blooming effect on the CCD induces a strong error in the intensity of the overlapping reflections. Additionally, particles might partially fall out of the illumination as no particle tracking was used during the data acquisition, inducing errors in the integration or distortion refinement process. These extrinsic effects accumulate with the intrinsic effects due to the change in beam energy that were discussed before.

To investigate these differences further, the final integration file for P1 was further analyzed. Figure 6-a depicts the ratio of the integrated intensity of the reflections to their standard uncertainties (I / sigma(I)) at both 30 kV and 200 kV for this particle. For resolutions higher than 0.4 $Å^{-1}$, which contains most of the reflections, there is no significant difference in the high versus low acceleration voltage. This shows that for both beam energies, the electron dose used results in sufficiently high reflection intensities. Nonetheless, the number of reflections slightly differs in different resolution shells between these datasets. Some reflections occur only in one dataset and not in the other one, denoted as unique reflections in Figure 6-b and Figure 6-c. The relative amount of such reflections occurring uniquely in one of the two

datasets increases with resolution. This is mainly due to the intrinsic difference in the radii of the Ewald sphere at low versus high acceleration voltage. The radius of the Ewald sphere is equivalent to the reciprocal of the electron beam wavelength. Table 2 lists wavelengths and their Ewald sphere radii for the acceleration voltages used in this study. The curvature of the Ewald sphere at 30 kV is 2.8 times higher than 200 kV. This is schematically illustrated in Figure 7 and is also evident in the frames (Figure 5). Ideally, the resolution would be infinite and there would be no missing wedge in the data. However, this is not the case experimentally. Even though the low-resolution reflections are cut by both Ewald spheres, reflections are sampled differently at higher resolutions. The chance of sampling higher-order Laue zones is higher at low acceleration voltages. This also means that the excitation conditions vary upon changing the acceleration voltage, leading to differences in the multiple scattering events. However, the number of these unique reflections is just 8.3% and 6.8% of the total reflections at 30 kV and 200 kV, respectively. Thus, they cannot cause a large R_{int} difference between 30 kV and 200 kV.

Therefore, this difference in R_{int} mainly originates from the intense multiple scattering at lower acceleration voltage. The mean free path (MFP) of an electron in matter highly depends on its energy. Figure 8 demonstrates the elastic and inelastic MFPs for $BaTiO_3$ as a function of the acceleration voltage, calculated based on Rutherford scattering [29]. Both inelastic and elastic mean free paths decrease dramatically as the acceleration voltage reduces. Thus, the probability of the scattering events is indeed increasing as the beam energy decreases, leading to a high R_{int} at lower acceleration voltages.

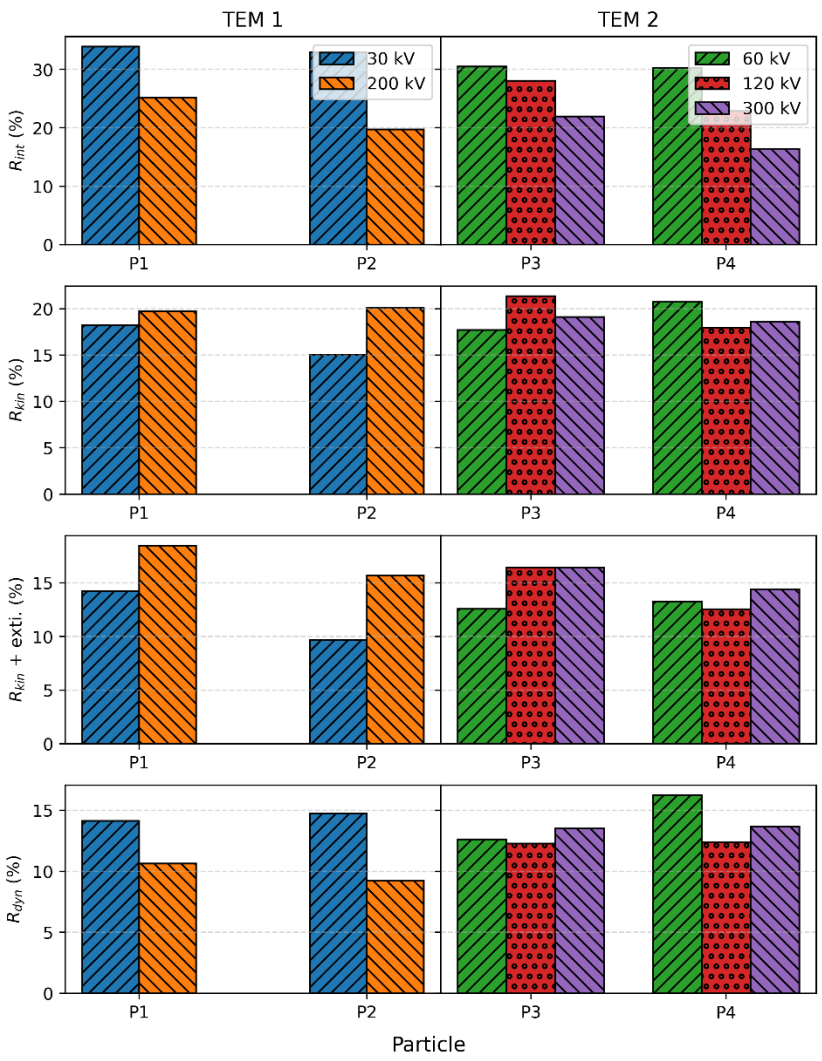

Figure 4. Agreement factors of the different particles after integration (R_{int}), kinematical refinement (R_{kin}), kinematical refinement with extinction correction (R_{kin} + exit.) and dynamical refinement (R_{dyn}).

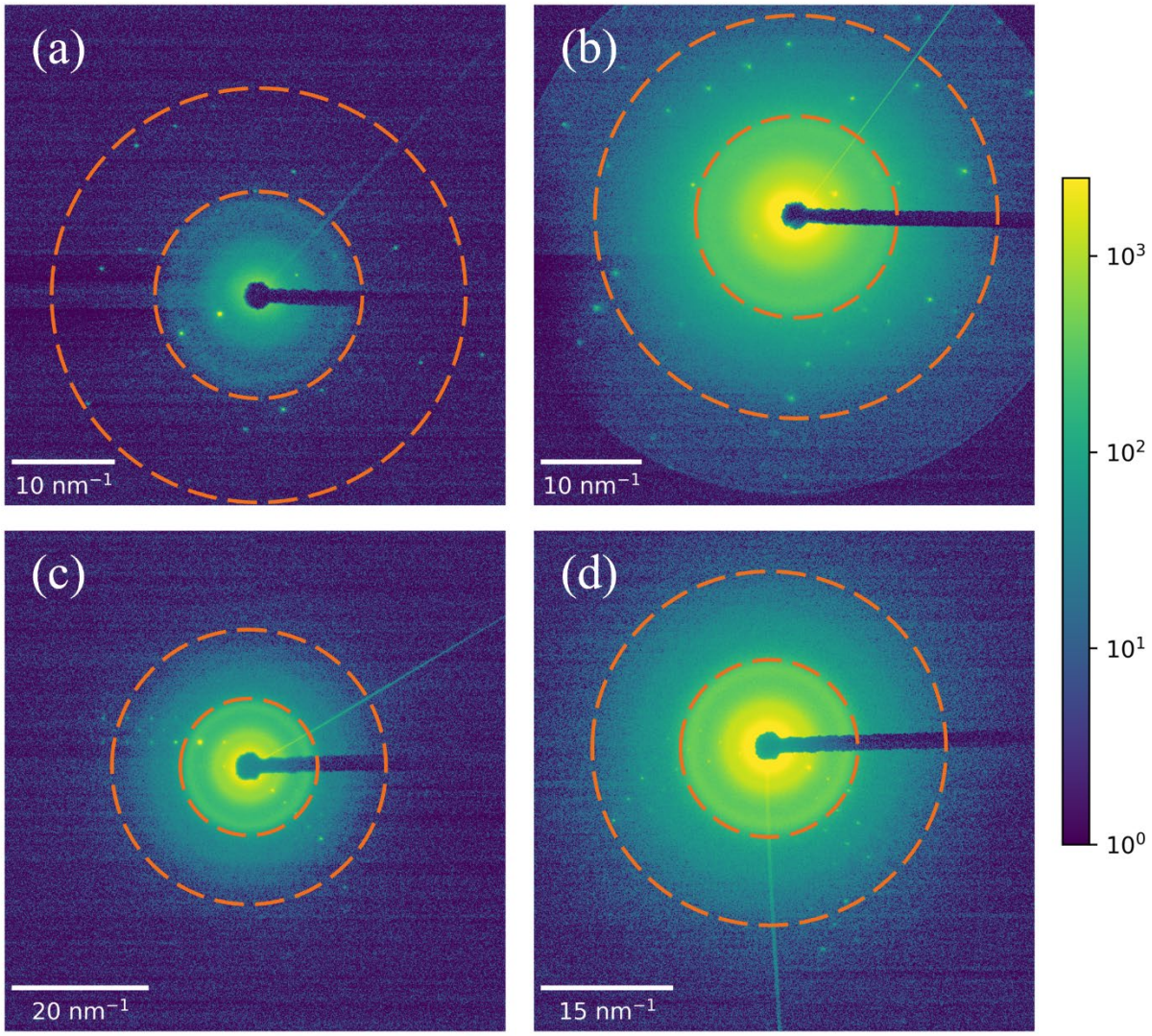

Figure 5. Similar diffraction patterns for P1 at 200 kV (a) and 30 kV (b) and for P3 at 300 kV (c) and 60 kV (d). For better visualization, the frames are plotted with a logarithmic scale and clipped at 2500 counts. The dashed circles show the resolution rings at 10 nm^{-1} (smaller circle) and 20 nm^{-1} (larger circle).

Table 2. The wavelength (λ) and Ewald sphere radius (R_{ES}) at different acceleration voltages.

HT (kV)	λ (pm)	R_{ES} (pm^{-1})
30	6.979	0.143
60	4.866	0.206
120	3.349	0.299
200	2.508	0.399
300	1.969	0.508

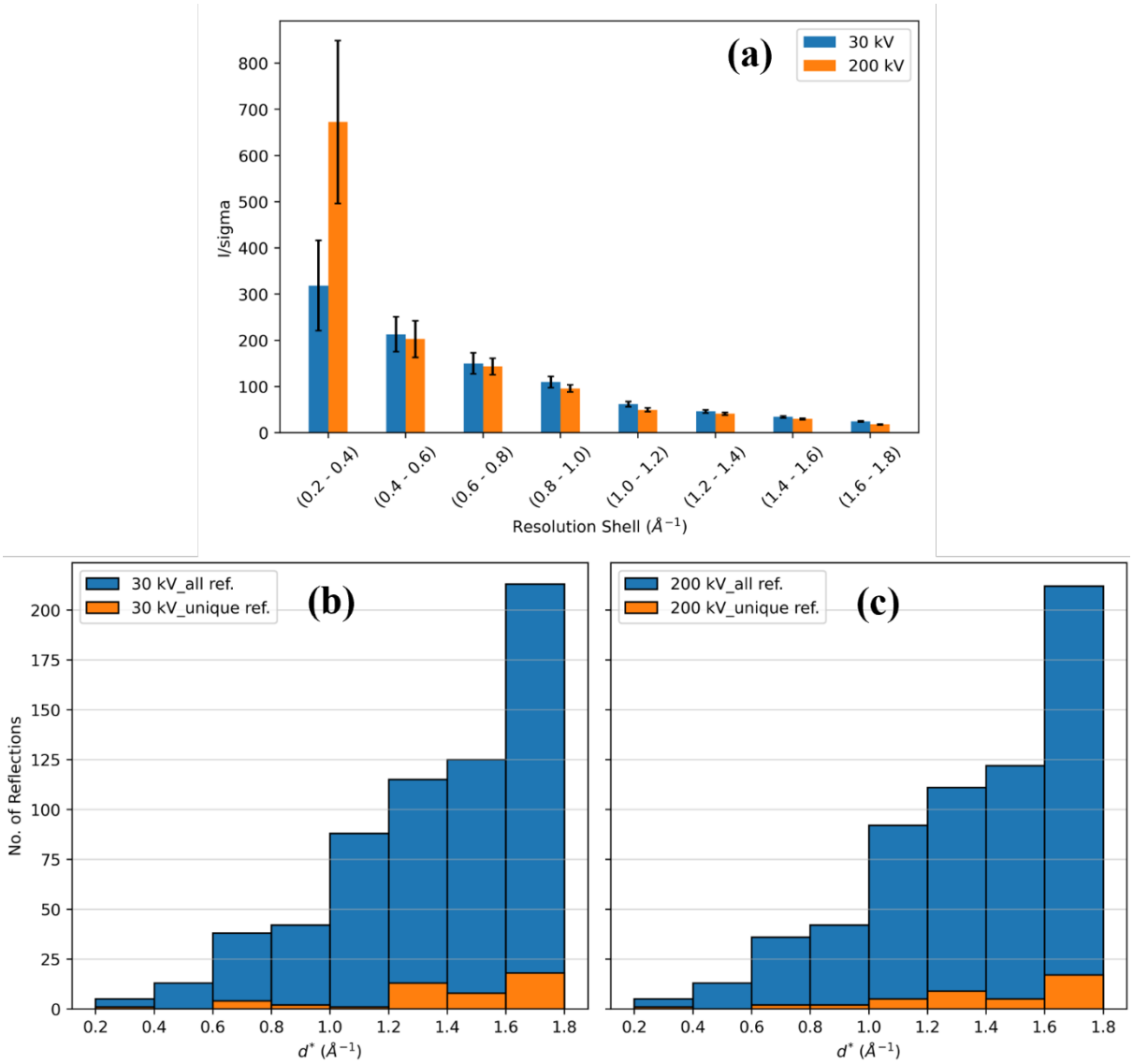

Figure 6. The average I/sig(I) for P1 (a), and the number of reflections after integration at 30 keV (b) and 200 keV (c). The number of unique reflections between these beam energies are depicted in orange.

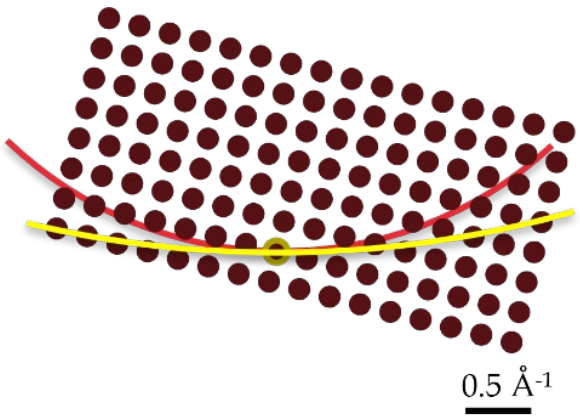

Figure 7. The curvature of the Ewald Sphere at 30 kV (red) and 200 kV(yellow).

3.2 Structure Solution and Refinement

After the integration process, reflections with I/sigma(I) higher than 2 were imported and symmetrically averaged for the solution and refinement stage. In all cases, a solution was found in the $Pm\bar{3}m$ space group. For P1 at both 30 kV and 200 kV and P3 at 120 kV, there was one extra oxygen atom close to the barium atom in the initial solution structure at an unrealistically close distance. These additional atoms were removed manually, before proceeding to the refinement process. In this structure, the refinement procedure only consists of refining the scale factor of the data and the atomic displacement parameters of the atoms, as all atoms occupy special positions. The atomic displacements were refined isotropically for all the atoms in this study, noted as U_{iso}. The R-factor between the structure factors of the refined model (F_c) and acquired data (F_o) was selected as a measure for the quality of the structure refinement, commonly known as R_{obs}. The refinement quality was compared at three different stages:

I. Refining the structure assuming a kinematical regime, annotated as R_{kin}
II. After introducing extinction correction to the first case, annotated as R_{kin} + exti.
III. After performing dynamical refinement on the first case, annotated as R_{dyn}

The results are plotted in Figure 4. In most cases, R_{kin} improved as the acceleration voltage decreased (Figure 4). Nonetheless, Barium U_{iso} was either negative or very small for all of the datasets (Figure 9). This is a common issue for heavy atoms during refinement without any constraints. Thus, a low R factor does not necessarily indicate a better refinement. In the next stage, the extinction correction was added to the refinement using the SHELX model. Extinction correction is normally used to correct the absorption of the beam in the crystal. For 3DED data, this correction can improve the agreement factor and correct negative atomic displacement parameters [21]. This correction decreased the R_{obs} of all datasets (R_{kin} + exti. in Figure 4) and resulted in positive U_{iso} values for Barium on all datasets. For datasets of the same particle, the improvement was significantly larger at the lower acceleration voltages (Figure 10). This can be due to the higher chance of inelastic interaction between the beam and the matter which can lead to higher absorption. Although the data at lower acceleration voltages show better agreement factors during the kinematical refinement in this study, drawing a general conclusion for comparing higher and lower energies seems rather naïve. First of all, as we mentioned earlier, R-factors are not necessarily a good indicator of the refinement quality, as the structure might not be meaningful. Secondly, the thickness of the sample can heavily affect 3DED results, as multiple scattering is going to intensify and dominate the diffraction signal. Moreover, the weakly accelerated electrons have less chance of passing through the sample. Nevertheless, our results imply that structure determination using 3DED is not only possible at low acceleration voltages, but it can also lead to comparable results upon having samples with suitable dimensions, even with kinematical refinement.

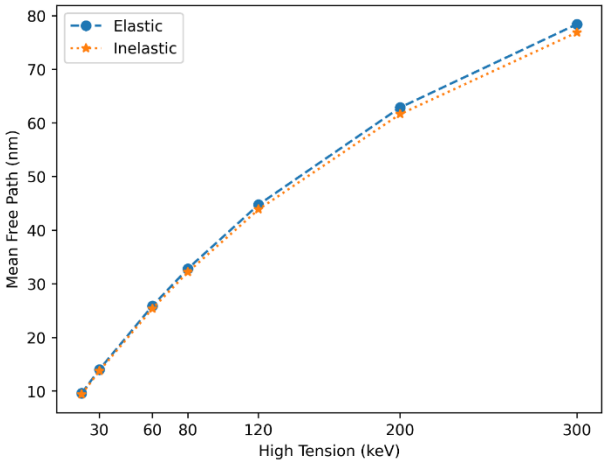

Figure 8. Elastic and inelastic Mean Free Paths (MFP) for $BaTiO_3$.

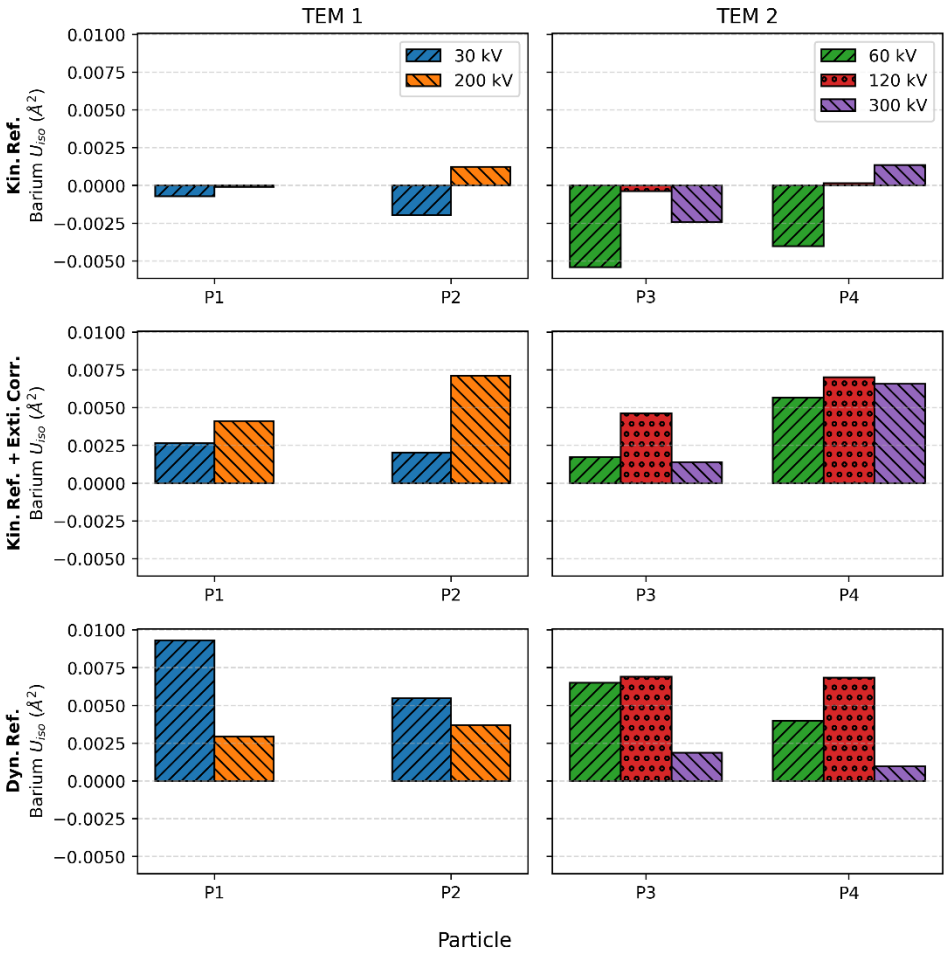

Figure 9. Barium U_{iso} after the refinement at different stages.

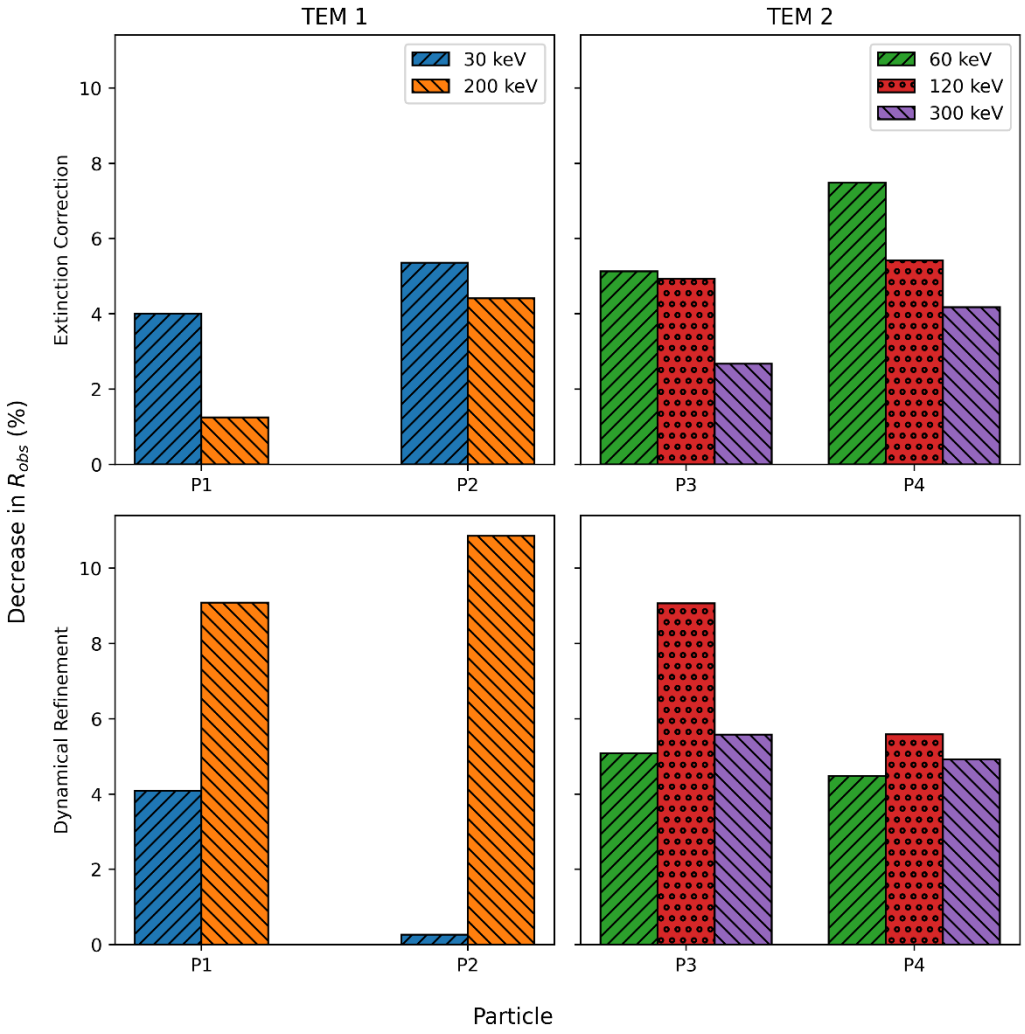

Figure 10. Decrease in R_{obs} after extinction correction and dynamical refinement.

At the final stage of the refinement, dynamical refinement was implemented on the kinematically refined data without extinction correction. The parameters for the dynamical calculations are listed in Table 3. As expected, R_{obs} decreased significantly in most of the cases (R_{dyn} in Figure 4). Nonetheless, the dynamical refinement seems to work best in intermediate to high acceleration voltages such as 120 kV, 200 kV, or 300 kV (Figure 10). Dynamical refinement also turned negative Barium U_{iso} to positive, meaningful values in all cases (Figure 9). It is important to note that, currently, the dynamical refinement only takes elastic scattering into account. Therefore, the calculations work best at higher acceleration voltages which have lower inelastic scattering.

Table 3. Parameters used for dynamical refinement.

Maximal diffraction vector g(max)	2
Maximal excitation error (Matrix)	0.01
Maximal excitation error (Refine)	0.1
R_{Sg} (max)	0.7
D_{Sg}	0.0014
Number of integration steps	40

4 Conclusions

3DED is an established technique for solving the structure of nanoparticles. In this study, we investigated the effect of the beam energy on the quality of the 3DED data acquired on $BaTiO_3$ nanoparticles. Beam energies ranged from 300 kV to 30 kV, covering high beam energies in conventional TEMs to lower beam energies as would be used in a conventional SEM. As expected, the distortions of the data intensify as the acceleration voltage decreases. This is because the distortion of the lenses depends on the acceleration voltage. Although distortion refinement works well on the 3DED data, R_{int} is still lower for datasets acquired at higher beam energies. This is mainly due to the higher dynamical scattering at lower beam energies. Nevertheless, the structure solution was successful in all cases. This highlights the abilities of 3DED which can be applied to data with different dynamical contributions. Additionally, this work shows the possibility of using this technique in the emerging STEM-in-SEM methods which collect diffraction patterns by installing detectors in SEMs at low beam energies.

The kinematical refinement surprisingly demonstrated lower residual factors for lower energies. However, U_{iso} became negative for the barium atom in almost all cases. This deficiency could be resolved by performing either extinction correction or dynamical refinement. The latter could noticeably decrease the agreement factor for higher beam energies. Currently, the dynamical calculations assume the electrons scatter elastically which is more suitable for high acceleration voltages.

Acknowledgments

The authors acknowledge funding from the Research Foundation Flanders (FWO, Belgium) project SBO S000121N. The authors are also grateful to Dr. Armand Béché and Dr. Lars Riekehr for their technical support and to Prof. Lukáš Palatinus, Dr. Stefano Canossa, Dr. Maria Batuk and Amirhossein Hajizadeh for fruitful discussions.

References

1. Gemmi, M., et al., *3D electron diffraction: the nanocrystallography revolution.* ACS Central Science, 2019. **5**(8): p. 1315-1329. https://doi.org/10.1021/acscentsci.9b00394
2. Nannenga, B.L. and T. Gonen, *The cryo-EM method microcrystal electron diffraction (MicroED).* Nature Methods, 2019. **16**(5): p. 369-379. https://doi.org/10.1038/s41592-019-0395-x
3. Klar, P.B., et al., *Accurate structure models and absolute configuration determination using dynamical effects in continuous-rotation 3D electron diffraction data.* Nature Chemistry, 2023. **15**(6): p. 848-855. https://doi.org/10.1038/s41557-023-01186-1
4. Gruene, T. and E. Mugnaioli, *3D Electron Diffraction for Chemical Analysis: Instrumentation Developments and Innovative Applications.* Chemical Reviews, 2021. **121**(19): p. 11823-11834. https://doi.org/10.1021/acs.chemrev.1c00207
5. Egerton, R.F., *Choice of operating voltage for a transmission electron microscope.* Ultramicroscopy, 2014. **145**: p. 85-93. https://doi.org/10.1016/j.ultramic.2013.10.019
6. Kohl, H. and L. Reimer, *Transmission Electron Microscopy*. Springer Series in Optical Sciences. Vol. 36. 2008. https://doi.org/10.1007/978-0-387-40093-8
7. Suosaari, E.P., et al., *Authigenic clays as precursors to carbonate precipitation in saline lakes of Salar de Llamara, Northern Chile.* Communications Earth & Environment, 2022. **3**(1): p. 325. https://doi.org/10.1038/s43247-022-00658-5
8. Mugnaioli, E., et al., *Wodegongjieite, ideally $KCa_3(Al_7Si_9)O_{32}$, a new sheet silicate isostructural with the feldspar polymorph kokchetavite, $KAlSi_3O_8$.* Mineralogical Magazine, 2022. **86**(6): p. 975-987. https://doi.org/10.1180/mgm.2022.107
9. Giacobbe, C., et al., *The crystal structure of the killer fibre erionite from Tuzköy (Cappadocia, Turkey).* IUCrJ, 2023. **10**(4). https://doi.org/10.1107/s2052252523003500
10. Zhou, H., et al., *Programming Conventional Electron Microscopes for Solving Ultrahigh-Resolution Structures of Small and Macro-Molecules.* Analytical Chemistry, 2019. **91**(17): p. 10996-11003. https://doi.org/10.1021/acs.analchem.9b01162
11. Martynowycz, M.W., et al., *Benchmarking the ideal sample thickness in cryo-EM.* Proceedings of the National Academy of Sciences, 2021. **118**(49): p. e2108884118. https://doi.org/10.1073/pnas.2108884118
12. Vainshtein, B., *Structure Analysis by Electron Diffraction (transl. by Feigl, E. and Spink, JA) Pergamon Press*. 1964, Oxford. https://doi.org/10.1016/C2013-0-01759-8
13. Dorset, D.L., *Is electron crystallography possible? The direct determination of organic crystal structures.* Ultramicroscopy, 1991. **38**(1): p. 23-40. https://doi.org/10.1016/0304-3991(91)90106-G
14. Carter, C.B. and D.B. Williams, *Transmission electron microscopy: Diffraction, imaging, and spectrometry*. 2016: Springer. https://doi.org/10.1007/978-3-319-26651-0
15. Brázda, P., et al., *Accurate lattice parameters from 3D electron diffraction data. I. Optical distortions.* IUCrJ, 2022. **9**(6). https://doi.org/10.1107/S2052252522007904
16. Clabbers, M.T., et al., *Electron diffraction data processing with DIALS.* Acta Crystallographica Section D: Structural Biology, 2018. **74**(6): p. 506-518. https://doi.org/10.1107/S2059798318007726
17. Mahr, C., et al., *Influence of distortions of recorded diffraction patterns on strain analysis by nano-beam electron diffraction.* Ultramicroscopy, 2019. **196**: p. 74-82. https://doi.org/10.1016/j.ultramic.2018.09.010
18. Ångström, J., H. Chen, and W. Wan, *Accurate lattice-parameter determination from electron diffraction tomography data using two-dimensional diffraction vectors.* Journal of Applied Crystallography, 2018. **51**(4): p. 982-989.

https://doi.org/10.1107/S1600576718006635
19. Egerton, R., *Mechanisms of radiation damage in beam-sensitive specimens, for TEM accelerating voltages between 10 and 300 kV.* Microscopy research and technique, 2012. **75**(11): p. 1550-1556. https://doi.org/10.1002/jemt.22099
20. Latychevskaia, T. and J.P. Abrahams, *Inelastic scattering and solvent scattering reduce dynamical diffraction in biological crystals.* Acta Crystallographica Section B: Structural Science, Crystal Engineering and Materials, 2019. **75**(4): p. 523-531. https://doi.org/10.1107/S2052520619009661
21. Yang, T., H. Xu, and X. Zou, *Improving data quality for three-dimensional electron diffraction by a post-column energy filter and a new crystal tracking method.* Journal of applied crystallography, 2022. **55**(6). https://doi.org/10.1107/S1600576722009633
22. Cabaj, M., et al., *The influence of energy filtering on kinematical and dynamical structure refinement from 3D ED data.* Acta Crystallographica Section A: Foundations of Crystallography, 2023. **78**: p. a619-a619.
23. De La Peña, F., et al., *hyperspy/hyperspy: Release v1. 7.3.* Zenodo.
24. Palatinus, L., et al., *Specifics of the data processing of precession electron diffraction tomography data and their implementation in the program PETS2. 0.* Acta Crystallographica Section B: Structural Science, Crystal Engineering and Materials, 2019. **75**(4): p. 512-522. https://doi.org/10.1107/S2052520619007534
25. Palatinus, L. and G. Chapuis, *SUPERFLIP–a computer program for the solution of crystal structures by charge flipping in arbitrary dimensions.* Journal of Applied Crystallography, 2007. **40**(4): p. 786-790. https://doi.org/10.1107/S0021889807029238
26. Petříček, V., et al., *Jana2020 – a new version of the crystallographic computing system Jana.* Zeitschrift für Kristallographie - Crystalline Materials, 2023. https://doi.org/doi:10.1515/zkri-2023-0005
27. Smith, M.B., et al., *Crystal structure and the paraelectric-to-ferroelectric phase transition of nanoscale BaTiO3.* Journal of the American Chemical Society, 2008. **130**(22): p. 6955-6963. https://doi.org/10.1021/ja0758436
28. Kim, S.-D., et al., *Inverse size-dependence of piezoelectricity in single BaTiO3 nanoparticles.* Nano Energy, 2019. **58**: p. 78-84. https://doi.org/10.1016/j.nanoen.2018.12.096
29. Gorelik, T.E., et al., *Towards quantitative treatment of electron pair distribution function.* Acta Crystallographica Section B: Structural Science, Crystal Engineering and Materials, 2019. **75**(4): p. 532-549. https://doi.org/10.1107/S205252061900670X

Supplementary Information

The tetragonality (c/a) of $BaTiO_3$ nanoparticles arises from the slight displacement of the titanium atom from the center of the unit cell, which breaks the cubic symmetry [1]. The amount of this displacement depends on the size of the nanoparticle. For instance, based on synchrotron X-ray diffraction data, the titanium atom is displaced 0.018 Å, 0.024 and 0.034 Å for, respectively, 70-nm, 45-nm and 26-nm nanoparticles. Consequently, the space group transforms from $Pm\bar{3}m$ to $P4mm$. Additionally, the unit cell slightly changes turning to a tetragonal system. However, the tetragonality was only 1.0065, 1.0054 and 1.0044 for the mentioned particles, respectively. Nevertheless, the tetragonality of the unit cell is localized and not necessarily homogenous on the whole particle [2]. As 3DED merely provides overall information from the whole particle, the signal might not even reflect such minor localization effects in the average structure. Moreover, as the tetragonality of the unit cell is minute and there are already some distortions in the data, it is prone to errors in directly distinguishing the c-axis from the measured unit cell. Thus, the structure should be solved and refined in three configurations where each time one main axis of the found cell (a, b, or c) is set to be the unique axis of the tetragonal cell. In an ideal condition, it should not be possible to solve the structure in the wrong configurations.

To investigate the possibility of solving $BaTiO_3$ structure in the tetragonal phase using 3DED, the datasets acquired at 200 kV for P1 and P2 were selected to be further analyzed. This selection is because the distortions are lower at higher beam energies and the dynamical refinements showed better results at 200 kV compared to 300 kV. As the c-axis of the unit cell could be any of the found axes, the distortion refinements were performed on three different orientations. Each time, one axis was set as the unique axis of the tetragonal cell. These are denoted as, for instance, $P1_a$, $P1_b$, $P1_c$. Afterward, both Superflip and SHELXT [3] were tried for the structure solution and refinement. Similar to the cubic structure, the refinement was compared at three stages, i.e. kinematical refinement, kinematical refinement with extinction correction and dynamical refinement. The results were compared with the results for the cubic structure.

After the distortion refinements in the integration process, the tetragonality of the unit cells was calculated for each case (Table S1). Only $P1_a$ and $P2_c$ showed tetragonality higher than 1. Since the tetragonality has never been less than 1 in other studies, these two orientations could have the correct choice of the unique axis for the tetragonal cell. Nevertheless, both these values are still smaller than the measured tetragonality in similar studies. After the integration process, the structure solution was initially performed by Superflip. In all cases, the structure was solved in P4/mmm space group regardless of the choice of the unique axis. Moreover, except for $P2_a$, the resulting structure did not chemically make sense. SHLEXT, however, showed better results as it provided a reasonable structure solution in both P4/mmm and P4mm space groups. Nevertheless, the solution was not complete in most cases. The deficiencies of the solutions are listed in Table S2 for different tetragonal axes.

Table S1. The tetragonality of the unit cell for P1 at 200 kV, after distortion refinement by different c axis.

	P1			P2		
Tetragonal Axis	**a**	**b**	**c**	**a**	**b**	**c**
Tetragonality (c/a)	1.0012	0.9985	0.9976	0.9969	0.9992	1.0020

Table S2. Deficiencies of the structures solved by SHLEXT for P1 and P2 at 200 kV assuming different axes as the tetragonal axis.

Tetragonal Axis	**Structure Deficiency**
P1a	Missing one oxygen atom
P1b	Missing one oxygen atom
P1c	Missing one oxygen atom Assigned titanium to one oxygen atom
P2a	Missing one oxygen atom
P2b	Missing one oxygen atom Assigned titanium to one oxygen atom
P2c	None

Moreover, the structure refinement was not perfect. In all cases, there were *singularity* errors in the refinement of the oxygen positions in Jana. This indicates this parameter did not affect the refinement and was fixed. The refinement was continued skipping these errors and the results are plotted in Figure S1. None of the tetragonal solutions stands out in the results. Furthermore, the results for the cubic symmetry often stay very close to the best R factor in the tetragonal symmetries. The dislocation of the titanium atom was merely 0.015 ± 0.002 Å for the kinematical refinement, decreasing after the extinction correction and dynamical refinement to 0.011 Å and <0.003 Å, respectively. This negligible dislocation indicates that the effect of the localized tetragonality seems negligible on the 3DED data.

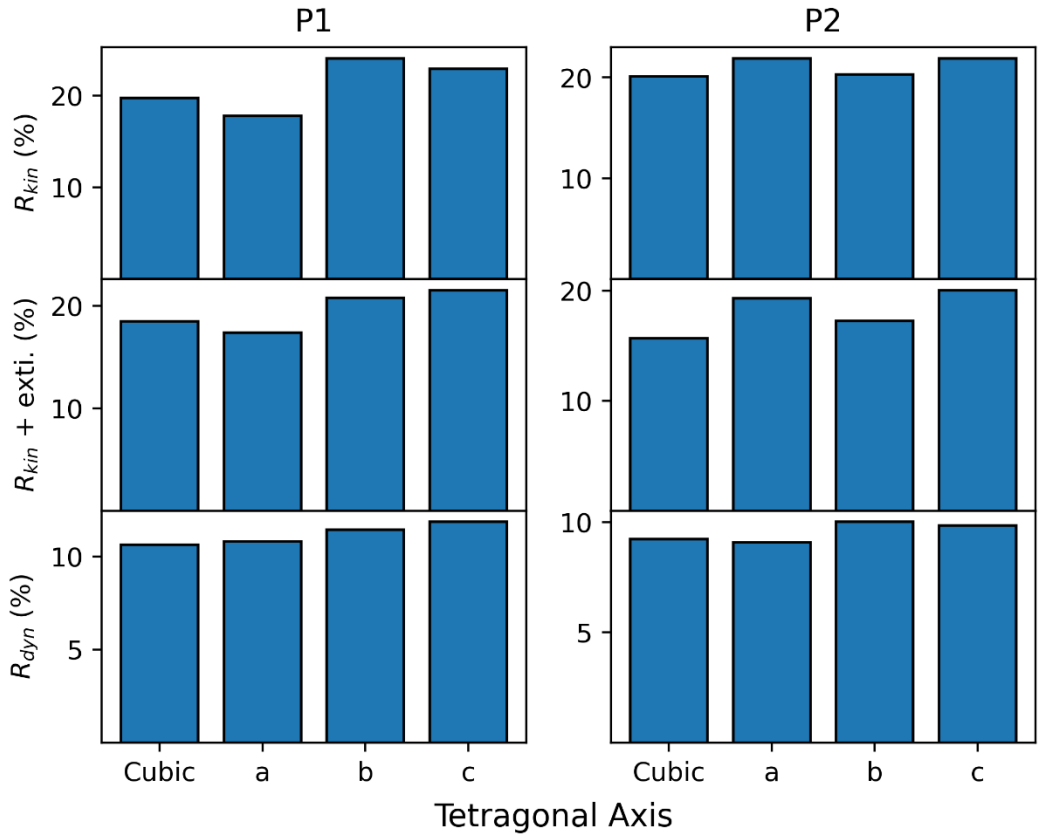

Figure S1. R factors for P1 and P2 at 200 kV after refining the tetragonal structure assuming different unique axes for the tetragonal cell. The first bar belongs to the cubic structure.

References

1. Smith, M.B., et al., *Crystal structure and the paraelectric-to-ferroelectric phase transition of nanoscale BaTiO3.* Journal of the American Chemical Society, 2008. **130**(22): p. 6955-6963. https://doi.org/10.1021/ja0758436
2. Kim, S.-D., et al., *Inverse size-dependence of piezoelectricity in single BaTiO3 nanoparticles.* Nano Energy, 2019. **58**: p. 78-84. https://doi.org/10.1016/j.nanoen.2018.12.096
3. Sheldrick, G.M., *SHELXT–Integrated space-group and crystal-structure determination.* Acta Crystallographica Section A: Foundations and Advances, 2015. **71**(1): p. 3-8. https://doi.org/10.1107/S2053273314026370